Predictive Control for Alleviation of Gust Loads on Very Flexible Aircraft

Robert J. S. Simpson*, Rafael Palacios† and Henrik Hesse‡

Imperial College, London, SW7 2AZ, United Kingdom

and

Paul Goulart§

Swiss Federal Institute of Technology (ETH), 8092 Zurich, Switzerland

In this work the dynamics of very flexible aircraft are described by a set of nonlinear, multi-disciplinary equations of motion. Primary structural components are represented by a geometrically-exact composite beam model which captures the large dynamic deformations of the aircraft and the interaction between rigid-body and elastic degrees-of-freedom. In addition, an implementation of the unsteady vortex-lattice method capable of handling arbitrary kinematics is used to capture the unsteady, three-dimensional flow-field around the aircraft as it deforms. Linearization of this coupled nonlinear description, which can in general be about a nonlinear reference state, is performed to yield relatively high-order linear time-invariant state-space models. Subsequent reduction of these models using standard balanced truncation results in low-order models suitable for the synthesis of online, optimization-based control schemes that incorporate actuator constraints. Predictive controllers are synthesized using these reduced-order models and applied to nonlinear simulations of the plant dynamics where they are shown to be superior to equivalent optimal linear controllers (LQR) for problems in which constraints are active.

*Graduate Student, Department of Aeronautics, 363A Roderic Hill Building; r.simpson11@imperial.ac.uk. AIAA Student Member.

†Senior Lecturer, Department of Aeronautics, 355 Roderic Hill Building; rpalacio@imperial.ac.uk. AIAA Member.

‡Post-Doctoral Researcher, Department of Aeronautics, 363A Roderic Hill Building; h.hesse09@imperial.ac.uk. AIAA Member.

§Senior Researcher, Automatic Control Laboratory; pgoulart@control.ee.ethz.ch.

Nomenclature

A	state-space system matrix
$\mathcal{A}$	aerodynamic influence coefficient matrix (downwash)
$\mathcal{A}_{\boldsymbol{U}}$	aerodynamic influence coefficient matrix (velocity)
b	semi-chord, m
Δb	panel span, m
C	constant sparse matrix / state-space output matrix
$\mathcal{C}$	tangent damping matrix
c	chord, m
Δc	panel chord, m
d	gust ordinate, m
E_x	mixed constraint matrix (states)
E_u	mixed constraint matrix (inputs)
F	terminal constraint matrix
H	control horizon
K	number of panels
K_ζ	number of grid points
K_{LQR}	linear quadratic regulator gain matrix
$\mathcal{K}$	tangent stiffness / MPC control law
k	discrete time step index / reduced frequency
l	number of outputs
m	number of inputs
M	number of chordwise panels
$\mathcal{M}$	mass matrix
N	number of spanwise panels
N_S	number of nodes in structural model
n	number of states / normal vector
P	state cost weighting matrix
Q	input cost weighting matrix / generalized nodal forces
R	terminal cost weighting matrix / beam nodal displacement, m
T	full- to reduced-state transformation
t	time, s
Δt	discrete time step, s
U	External fluid velocities, $\mathrm{m{\cdot}s^{-1}}$
U_{design}	design gust velocity, $\mathrm{m{\cdot}s^{-1}}$
U_g	vertical gust velocity, $\mathrm{m{\cdot}s^{-1}}$
U_∞	free-stream velocity magnitude, $\mathrm{m{\cdot}s^{-1}}$
u	system inputs
$\mathbf{u}$	control trajectory

v	velocity of body-fixed frame, $\mathrm{m \cdot s^{-1}}$
w	downwash at collocation points, $\mathrm{m \cdot s^{-1}}$
x	system states
$\mathbf{x}$	state trajectory
y	system outputs
β	rigid-body degrees-of-freedom / flap angle, rad
Γ	circulation, $\mathrm{m^2 \cdot s^{-1}}$
η	structural degrees of freedom
Θ	Euler angles, rad
ζ	aerodynamic grid coordinates
ρ_∞	free-stream air density, $\mathrm{kg \cdot m^{-3}}$
χ	quaternions
ω	angular velocity vector of body-fixed frame, $\mathrm{rad \cdot s^{-1}}$
ω_β	angular velocity of flap, $\mathrm{rad \cdot s^{-1}}$
$\mathbf{1}$	vector of ones

Subscript

$(\bullet)_0$	reference condition
$(\bullet)_g$	pertaining to the gust

Superscript

F	fluid degrees-of-freedom
R	rigid-body degrees-of-freedom
S	structural degrees-of-freedom
$(\bullet)^{ref}$	reference control trajectory
$(\dot{\bullet})$	time derivative
$(\hat{\bullet})$	pertaining to the reduced-order system
$(\bar{\bullet})$	linearized quantity
$(\bullet)^\star$	pertaining to the wake

I. Introduction

The desire for reduced fuel-burn due to commercial and environmental pressures, and the desire for extreme range and endurance capabilities of unmanned platforms, is forcing a paradigm shift in the design of next-generation aircraft. A common trend in these platforms is their ever-increasing structural flexibility, caused by low-weight, high-aspect-ratio designs, which has introduced significant complexity in the modeling process. Perhaps the foremost consequence of this is that vibration characteristics of very flexible aircraft (VFA) are of such low frequency that they interact with the classical flight dynamics response in a way that can only be described by a unified aeroelastic analysis incorporating rigid-body, elastic, and aerodynamics models simultaneously.[1,2] In addition to this, the aeroelastic trim configurations of VFA are far more sensitive to payload configuration[3] than that of conventional, stiff aircraft. Crucially, from a control perspective, the relatively-large static and dynamic deformations of VFA introduce state-dependent (and therefore temporal) variations of the aircraft dynamics. Thus, the assumption of a linear, time-invariant (LTI) system description, which is commonly found in the literature of flexible aircraft dynamics,[2,4] may not be appropriate when attempting to formulate suitable control strategies. Indeed, this point was strongly articulated in the report following the Helios mishap.[5]

Model predictive control (MPC) is a nonlinear control strategy, developed originally for the process industries, that is capable of handling multiple-input multiple-output (MIMO) systems naturally; enforcing constraints on linear functions of system inputs, input rates, and states; accounting for unmodeled plant dynamics and nonlinearities; and, dealing with uncertainties in the system input and/or output in a robust way.[6,7] It therefore offers an attractive solution to the challenging control problems inherent in flexible aircraft design and operation.

Recently, an MPC scheme for gust load alleviation was formulated using a linear, aeroelastic, reduced-order model (ROM) of a commercial airliner.[8] The proposed solution also included preview information of the future gust environment, provided by light detection and ranging sensors (LIDAR). When the controller was applied to the linear, full-order model it showed superior performance to that of a linear reference controller. A similar comparison was made by Haghighat *et al.*,[9] who showed that MPC with a prediction enhancement based on output disturbance feedback was more effective than a linear quadratic regulator (LQR) when applied to a linearized flexible aircraft model. The robustness of the MPC scheme was emphasized by successfully applying the same controller to a plant whose control effectiveness was reduced by 50%.

For very flexible vehicles, the system dynamics need to include nonlinear effects due to large geometry changes. Attempts to design active gust alleviation mechanisms on such plat-

forms have so far been restricted to the use of linear controllers obtained from linearization of vehicle dynamics around a reference condition. Cook *et al.*[10] and Dillsaver *et al.*[11] applied $\mathcal{H}_\infty$ and LQG controllers, respectively, to full aircraft models and investigated the response to gust and continuous disturbances. They have highlighted the difficulty of achieving robust control with linear control schemes on very flexible vehicles subject to large disturbances. In particular, the offline tuning of parameters used to ensure bounds on the plant states and inputs is not robust in the presence of significant plant nonlinearity or larger than expected exogenous disturbances. Since constraints are included in the online optimization problem posed during MPC, and since the controller may react in a nonlinear fashion when in proximity to these constraints, it is likely that predictive control will be superior to optimal linear control in challenging situations.

In this work reduced-order models of VFA dynamics are obtained from linearization of the full-order, nonlinear equations of motion that are used as a high-fidelity simulation of the plant dynamics. The reduced-order models are then used to synthesize model predictive controllers and equivalent linear quadratic regulators (LQRs) for application to the nonlinear plant. Nonlinear, linear and reduced-order modeling of the dynamics of flexible aircraft is therefore set out in Sec. II, followed by the control methodologies in Sec. III. Comparisons of nonlinear and linearized models, and models obtained from systematic model reduction, are shown in Sec. IV.B in which suitable reduced models for predictive control synthesis are identified. Discussion of closed-loop and controller performance on the nonlinear plant are then presented in Sec. IV.C.

II. Flexible Aircraft Flight Dynamics Modeling

The nonlinear, multidisciplinary analysis presented in this work is implemented in a Python-based framework called Simulation of High-Aspect-Ratio Planes in Python (SHARPy). In SHARPy, full flexible aircraft flight dynamics analysis is achieved by coupling a nonlinear, flexible-body dynamics, composite beam model with a geometrically-nonlinear implementation of the unsteady vortex-lattice method (UVLM). The nonlinear model, which will be referred to as the *plant*, is described in Sec. II.A and II.B. A linearization of this coupled model, and the re-casting of its underlying equations into state-space form, is the first step towards obtaining LTI systems useful for control synthesis, and is presented in Sec. II.C. For the purposes of MPC, where faster than real-time prediction of plant dynamics is required, it is necessary to reduce the size of the linear model; the model reduction process is therefore described in the final subsection (Sec. II.D).

A. Nonlinear Flexible-Body Dynamics

A geometrically-exact composite beam finite-element model based on the formulations by Hodges[12] and Géradin & Cardona[13] is used which is capable of capturing the dynamics of flexible, unconstrained structures subject to large geometrically-nonlinear deformations and nonlinear rigid-body motions. A moving body-fixed reference system, denoted the a-frame, is used to describe elastic deformations as well as the rigid-body motion of the structure. The discretized equations of motion (EoM) of a moving flexible body subject to external forces are[14]

$$\mathcal{M}(\eta)\begin{Bmatrix}\ddot{\eta}\\ \dot{\beta}\end{Bmatrix} + Q_{gyr}(\eta,\dot{\eta},\beta) + Q_{stiff}(\eta) = Q_{ext}(\eta,\dot{\eta},\beta,\chi), \tag{1}$$

where the structural degrees of freedom are denoted $\eta \in \mathbb{R}^{6(N_S-1)}$, where N_S is the number of nodes in the structural finite-element model. These degrees-of-freedom are the nodal displacements, R, and orientations of local nodal reference frames, denoted as B-frames, parameterized using the Cartesian Rotation Vector (CRV).[13] The rigid-body states, $\beta \in \mathbb{R}^6$, include the translational and angular velocities of the origin of the body-fixed reference frame, denoted v and ω respectively, as shown in Figure 1. The system dynamics are coupled through the tangent mass matrix, $\mathcal{M}(\eta)$, and the discrete gyroscopic and external forces, Q_{gyr} and Q_{ext}, respectively. Elastic forces, Q_{stiff}, are in general a nonlinear function of the elastic deformations, η. The structural and rigid-body components (denoted by superscripts S and R, respectively) of the gyroscopic, elastic and external forces can be identified as

$$Q_{gyr} = \begin{Bmatrix}Q^S_{gyr}\\ Q^R_{gyr}\end{Bmatrix}, \quad Q_{stiff} = \begin{Bmatrix}Q^S_{stiff}\\ 0\end{Bmatrix}, \quad \text{and} \quad Q_{ext} = \begin{Bmatrix}Q^S_{ext}\\ Q^R_{ext}\end{Bmatrix} \tag{2}$$

respectively. A more detailed description of the various terms in Eqs. (1) and (2) can be found in previous work by the authors.[14] At last, the orientation of the body-fixed reference frame with respect to an inertial frame is parameterized using quaternions, denoted by χ, by solving an extra set of attitude EoM.[15,16] Together with the Eq. (1) this completes the geometrically nonlinear description of the aircraft structural dynamics and nonlinear rigid-body motion.

B. Nonlinear, Three-Dimensional, Unsteady Aerodynamics

Assuming coincident spanwise discretizations, an aerodynamic lattice, ζ, is constructed that represents the aircraft lifting surfaces. From this discretization, the 3-D, time-domain, geometrically-nonlinear, unsteady aerodynamic loading is obtained using the unsteady vortex-lattice method. In the UVLM, quadrilateral vortex ring elements are used to discretize both

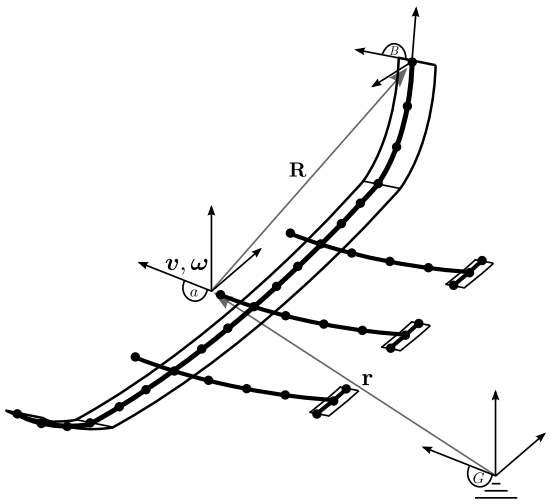

Figure 1. *HALE aircraft represented by lifting-surfaces and beams. The frames of reference used to build the FAFD model are shown.*

lifting surfaces and their wakes. Each surface (bound) vortex ring has an associated scalar circulation strength, Γ_{ij}, and a collocation point at which the non-penetration boundary condition is satisfied. Figure 2 depicts the vortex lattice geometry, ζ, where each collocation point is marked with a cross, and M and N are the number of chordwise and spanwise panels, respectively.

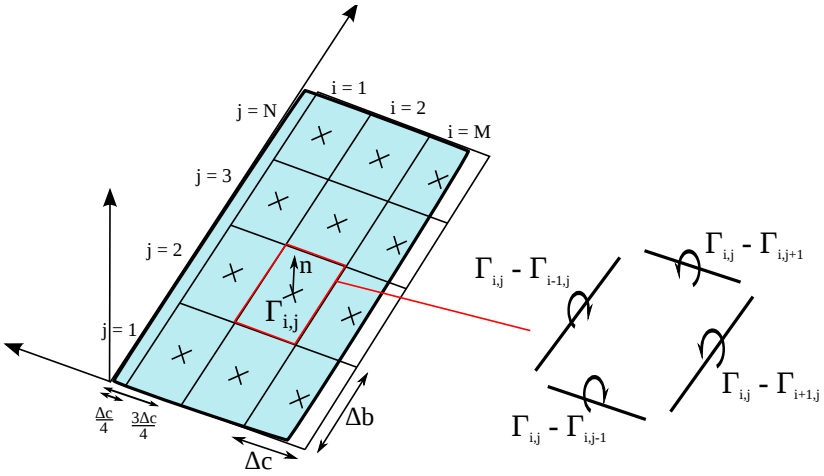

Figure 2. *Body surface overlaid with vortex lattice geometry. Four vortex segments are shown on the right, which have circulation strengths equal to the difference in adjacent vortex ring strengths.*

The Kutta condition and Joukowski hypothesis[17] are approximatley satisfied by shedding wake vortex rings from the trailing-edge of each surface every time step. A commonly used first-order, explicit, time-stepping scheme is employed.[18–20] This results in a time-varying,

discrete-time system of equations of the form

$$\mathcal{A}(\zeta)\Gamma_{k+1} + \mathcal{A}^\star(\zeta,\zeta^\star)\Gamma^\star_{k+1} + w_{k+1} = 0, \tag{3}$$

$$\Gamma^\star_{k+1} = C_\Gamma \Gamma_k + C^\star_\Gamma \Gamma^\star_k, \tag{4}$$

$$\zeta^\star_{k+1} - C_\zeta \zeta_{k+1} = C^\star_\zeta \zeta^\star_k + \Delta t\left(\mathcal{A}_{\boldsymbol{U}}\Gamma_k + \mathcal{A}^\star_{\boldsymbol{U}}\Gamma^\star_k\right) + \Delta t U^\star_k \ , \tag{5}$$

where Eq.(3) enforces the non-penetration boundary condition on the aircraft geometry, and Eqs. (4) & (5) propagate the wake circulation strength and wake geometry, respectively, through time. Note that the $(\,)^\star$ superscript denotes a state belonging to the aircraft wake, and the subscripts $(\,)_k$ and $(\,)_{k+1}$ refer to discrete time steps. $\Gamma \in \mathbb{R}^K$ is the vector of bound vortex ring strengths, where $K = MN$. Similarly, $\Gamma^\star \in \mathbb{R}^{K^\star}$ is the vector of wake circulation strengths where $K^\star = M^\star N$ and $M^\star$ is the number of chordwise panels in the wake. The downwash at the collocation points, $w \in \mathbb{R}^K$, is given by $w = W\left[-\dot{\zeta} + U\right]$, where $U \in \mathbb{R}^{3K_\zeta}$ are fluid velocities at the surface grid points which may include free-stream velocities and gusts. The matrix $W(\zeta_{k+1})$ interpolates from grid corner-points to collocation points and projects the resulting velocities along the corresponding panel normal vector. The final system state of interest is the wake lattice geometry, $\zeta^\star \in \mathbb{R}^{3K^\star_\zeta}$, where $K^\star_\zeta = (M^\star+1)(N+1)$ is the number of aerodynamic grid points in the wake. A more detailed description of the matrices in (3) - (5) can be found in previous work by the first two authors.[21]

The circulation distribution on the deformed aircraft is then post-processed to obtain the aerodynamic loading which is then mapped back onto the structural nodes. Thus the flexible-body dynamics and aerodynamics models are coupled to form a nonlinear aeroelastic model of the dynamics of flexible aircraft. In the presence of geometrically nonlinear deformations and complex kinematics care must be taken when post-processing the aircraft states to obtain the aerodynamic loading. In particular, the vector form of Joukowski's theorem must be used to yield induced drag results that properly account for leading-edge suction effects.[22]

C. Linearized Flexible Aircraft Dynamics

The structural dynamics are linearized around a point referred to as $(\eta_0, \dot{\eta}_0, \beta_0, \Theta_0)$ and small changes from this state will be represented with over-bars, that is, $(\bar{\eta}, \dot{\bar{\eta}}, \bar{\beta}, \bar{\Theta})$. The linearized (incremental) form of Eq. (1) around this point is[14]

$$\mathcal{M}(\eta_0)\begin{Bmatrix}\ddot{\bar{\eta}}\\ \dot{\bar{\beta}}\end{Bmatrix} + \mathcal{C}(\eta_0,\dot{\eta}_0,\beta_0)\begin{Bmatrix}\dot{\bar{\eta}}\\ \bar{\beta}\end{Bmatrix} + \mathcal{K}(\eta_0,\dot{\eta}_0,\beta_0)\begin{Bmatrix}\bar{\eta}\\ 0\end{Bmatrix} = \bar{Q}_{ext}\left(\bar{\eta},\dot{\bar{\eta}},\bar{\beta},\bar{\Theta}\right), \tag{6}$$

where the constant tangent damping and stiffness matrices $\mathcal{C}$ and $\mathcal{K}$, respectively, are obtained through direct linearization of the discretized forces in Eq. (1). Note that Euler

angles, Θ, are preferred in the linear analysis to describe variations of the a-frame orientation.[10] Projection of these linear EoM on the vibration modes of the unconstrained aircraft can further simplify the structural representation of the vehicle dynamics. In this work however, this linear, second-order set of ODEs is discretized in time using the Newmark-β scheme,[23] and cast in discrete-time state-space form. Following this the model is coupled with a linearized UVLM aerodynamics model to form a monolithic LTI state-space description of VFA dynamics which can in general be around a nonlinear reference condition.

The linearized form of the aerodynamics model is constructed using the model developed by Murua *et al.*[24] based on the description by Hall.[25] To obtain the state-space form of the UVLM, the governing equations are linearized on a frozen aerodynamic geometry around the aircraft trim condition, which may include large wing deformations and a non-planar wake. Therefore, the system of Eqs. (3)-(5) is reduced to

$$\mathcal{A}(\zeta_0)\bar{\Gamma}_{k+1} + \mathcal{A}(\zeta_0, \zeta_0^\star)^\star \bar{\Gamma}^\star_{k+1} + \bar{w}_{k+1} = 0, \tag{7}$$

$$\bar{\Gamma}^\star_{k+1} = C_\Gamma \bar{\Gamma}_k + C^\star_\Gamma \bar{\Gamma}^\star_k, \tag{8}$$

where the over-bars represent increments on the states about which the aircraft is linearized. The aerodynamic equations above are coupled with the linear structural Eqs. (6) and cast in the discrete-time state-space form

$$\begin{aligned} x(k+1) &= Ax(k) + Bu(k) + B_g u_g(k), \\ y(k) &= Cx(k), \end{aligned} \tag{9}$$

where u are the actuator inputs and subscript-g terms correspond to gust inputs. The state vector that completely determines the linear system is

$$x := (x_F;\ x_S;\ x_R)\,, \tag{10}$$

where

$$x_F := (\bar{\Gamma};\ \bar{\Gamma}^\star;\ \dot{\bar{\Gamma}}), \tag{11}$$

$$x_S := (\bar{\eta};\ \dot{\bar{\eta}})\,, \tag{12}$$

$$x_R := \left(\bar{\beta};\ \bar{\Theta}\right). \tag{13}$$

Note that the over-bars present in Eqs. (6)-(8) have been omitted for clarity. However, the linear states x are incremental and must be superimposed on the reference states. Also note that the time-rate-of-change of the vortex ring strengths, $\dot{\Gamma} \in \mathbb{R}^K$, are included in the state vector as it is required for the computation of unsteady aerodynamic loads.[24] Depending

on the finite-element discretization of the structural and aerodynamic models the number of states in Eq. (9) may be large, typically $\mathcal{O}(10^4)$ for converged discretizations. This set of coupled linear EoMs now form the basis for stability analyses, model reduction, and control syntheses.

D. Reduced-Order Models

Starting from the relatively-large linear model of Eq. (9) a reduced-order model is obtained for use in predictive control schemes or offline synthesis of optimal linear controllers. In either case it is useful to have a low-order representation of the system dynamics, however it is necessary for MPC in which faster-than-real-time optimization of the system dynamics must be achieved. To find a low-order representation, a new basis for the linear system of Eq. (9) is found in which the states are ranked in terms of their contribution to the input-output behavior of the system using balanced realization.[26,27] The first $\hat{n}$ balanced states are then preserved and the rest truncated. Choosing $\hat{n}$ is done by systematically reducing the order of the model whilst ensuring the frequency- and time- domain behaviour remains close to that of the full-order model. This standard balanced realization and truncation results in a full-state to reduced-state transformation

$$\hat{x} = Tx, \tag{14}$$

where $x \in \mathbb{R}^n$ are the full-order states, $T \in \mathbb{R}^{\hat{n}\times n}$ is the truncated balancing matrix, and $\hat{x} \in \mathbb{R}^{\hat{n}}$ are the reduced-order states associated with a truncation of the balanced system. The corresponding reduced-order state and output equations are

$$\begin{aligned} \hat{x}(k+1) &= \hat{A}\hat{x}(k) + \hat{B}u(k) + \hat{B}_g u_g(k), \\ y(k) &= \hat{C}\hat{x}(k), \end{aligned} \tag{15}$$

where $u \in \mathbb{R}^m$ and $u_g \in \mathbb{R}^{m_g}$ are the control inputs and gust inputs respectively. The matrices $\hat{A}$, $\hat{B}$, $\hat{B}_g$ and $\hat{C}$ are of size $\hat{n}\times\hat{n}$, $\hat{n}\times m$, $\hat{n}\times m_g$, and $l\times\hat{n}$ respectively, where l is the number of outputs.

III. Model Predictive Control Methodology

The model predictive control (MPC) scheme presented here results in a time-invariant implicit control law, $\mathcal{K}(\hat{x}, \hat{\mathbf{x}}^{ref}, \mathbf{u}^{ref})$, where $\hat{\mathbf{x}}^{ref} = \left\{\hat{x}_0^{ref}, \ldots, \hat{x}_{H-1}^{ref}\right\}$ and $\mathbf{u}^{ref} = \left\{u_0^{ref}, \ldots, u_{H-1}^{ref}\right\}$, where the integer $H \geq 2$ is the number of steps in the prediction horizon. This control law is defined as the first control action in the series of actions found by online solution of the

optimization problem

$$\min_{\hat{x}_i,\ u_i} \sum_{i=0}^{H-1} \left(\left|\left| \hat{x}_i - \hat{x}_i^{ref} \right|\right|_Q^2 + \left|\left| u_i - u_i^{ref} \right|\right|_R^2 \right) + \left|\left| \hat{x}_H - \hat{x}_H^{ref} \right|\right|_P^2 \tag{16}$$

s.t.

$$\hat{x}_{i+1} = \hat{A}\hat{x}_i + \hat{B}u_i \tag{17}$$

$$\hat{x}_0 = \hat{x}(k) \tag{18}$$

$$E_x x_i + E_u u_i \leq \mathbf{1} \quad \forall\ i = 0,\ ...,\ H-1 \tag{19}$$

$$F x_H \leq \mathbf{1} \tag{20}$$

where the matrices Q, R, and P are the state, input, and terminal cost weighting matrices, respectively. Eq. (17) contains the dynamics of the system and is simply the reduced-order, state-space description of Eq. (15) with gust inputs removed. The initial reduced-state is measured at the current discrete time step, Eq. (18), under the assumption that full-state feedback is available from the nonlinear plant and that the full- to reduced-order transformation of Eq. (14) is valid. In the case where the plant is nonlinear, which is to be expected, or in the case of unknown disturbances to the plant input and output, offset-free tracking is facilitated by comparing the measured plant state with the current state as predicted at the previous time-step. The resulting error is assumed to be constant along the prediction horizon and the reference trajectory is augmented to reflect this.[7]

Mixed constraints are specified with matrices E_x and E_u, which are typically sparse. Constraints specified on the inputs alone are hard limited, while input rate constraints are softened and can be formulated using Eq. (19) by introducing an auxiliary state[7] for each input rate that is to be constrained. In addition, the terminal state, $\hat{x}_H$, is constrained to lie within the polyhedron defined by the matrix F and the vector of ones, $\mathbf{1}$, by Eq. (20).

Currently, the MPC optimization problem of Eqs. (16) - (20) is cast in the form of a general quadratic programming (QP) problem using the open-source package μAO-MPC.[28] In their Python-based implementation the Hessian matrix, gradient vector, and constraint equations associated with the optimization of Eqs. (16) - (20) are calculated by considering the problem in condensed form. In addition to this, μAO-MPC automatically generates library-free C-code to solve the condensed problem. The result is an extremely fast, low-memory implementation (the original intended application was for microcontrollers). An Augmented-Lagrangian approach using a fixed number of iterations is used to solve the optimization in (nearly) deterministic time, and although the result may be sub-optimal it is still likely to give good controller performance.[28]

In addition to predictive control, equivalent linear quadratic regulators (LQRs) are synthesized using the same Q and R matrices as in Eq. (16). The optimization problem in LQR

control is simply an infinite-horizon unconstrained version of Eq. (16), i.e

$$\min_{\hat{x}_i,\ u_i} \sum_{i=0}^{\infty} \left(\left|\left| \hat{x}_i - \hat{x}_i^{ref} \right|\right|_Q^2 + \left|\left| u_i - u_i^{ref} \right|\right|_R^2 \right) \tag{21}$$

s.t.

$$\hat{x}_{i+1} = \hat{A}\hat{x}_i + \hat{B}u_i$$

$$\hat{x}_0 = \hat{x}(k)$$

where $H \to \infty$ and the terminal cost and constraints, and mixed constraints, are no longer present. Solution of this problem yields a constant optimal gain matrix, K_{LQR} and corresponding control action $u_{LQR}(\hat{x}) = -K_{LQR}\ \hat{x}$. For comparison of relative closed-loop performance, when input constraints are present in an MPC control law the corresponding LQR controller is saturated.

IV. Numerical Studies and Discussion

In order to test the nonlinear, linearized and reduced-order modeling approaches described above, and the synthesis and application of predictive controllers for gust load alleviation using these models, a cantilever wing test case is used based on the aeroelastic wing model introduced by Goland.[29,30] The relevant structural properties of the Goland wing are presented in Table 1, alongside details of the reference flow conditions and control system design. Because the wing centre-of-gravity is aft of its elastic axis the Goland wing experiences flutter instability at a free-stream velocity of around 170 m·s^{-1}.[20,21] To avoid complications associated with this instability the free-stream velocity is set as 140 m·s^{-1} for this study. In addition, the wing is subjected to vertical "$1-\cos$" gusts – details of these gusts, the open-loop response, and identification of a worst-case gust are presented in Sec. IV.A. Identification of reduced-order models (ROMs) suitable for synthesis of predictive control schemes are then presented in Sec. IV.B. Finally, the capabilities of predictive and LQR control schemes synthesized using these reduced-models are tested in nonlinear, closed-loop simulations of the plant in Sec. IV.C.

A. Open-Loop Response

The Goland wing is subjected to the "$1-\cos$" family of gusts described in Federal Aviation Regulation (FAR) §25.341, which are of the form

$$U_g = \frac{U_{design}}{2}\left(1 - \cos\left(\frac{2\pi d}{L_g}\right)\right), \quad \text{where } 0 \le d \le L_g, \tag{22}$$

Chord	1.8288 m
Semi-span	6.096 m
Elastic axis	33% chord
Center of gravity	43% chord
Mass per unit length	35.71 kg/m
Moment of inertia	8.64 kg·m
Torsional stiffness	0.99×10^6 N·m^2
Bending stiffness	9.77×10^6 N·m^2
Free stream velocity	140 m·s^{-1}
Angle-of-attack	0 deg
Air density	1.02 kg·m^{-3}
Control surfaces	1 TE flap at tip
Flap size	25% chord, 20% span
Measurements	root torsion and bending strains
Sampling interval, Δt	1.633×10^{-3} s
Model discretization	$M = 8$, $N = 20$

Table 1. Goland wing properties,[29] reference condition and control system details.

and U_g is the vertical gust velocity, U_{design} is the design gust velocity, and d is the distance into the gust which has length L_g. The largest design gust velocity in the requirements, $U_{design} = 17.07$ m·s^{-1}, was chosen for open-loop tests at a range of gust lengths, the results of which are shown in Figure 3.

Results of the linearized model, shown in Figure 3(a), show the root strains in torsion and bending due to gusts with lengths in the range 10 - 80m. Results from a 10m gust are shown because the high-frequency content of such disturbances excites the relatively stiff torsional degrees-of-freedom of the Goland wing and produces the maximum torsional strain of all the gust lengths investigated. The critical gust for maximum bending strain was found to be approximately 20m, and will be referred to as the critical gust length. Gust lengths of 60m and above produced a response that was effectively quasi-static, with minimal oscillatory behaviour and lower peak strains than the critical case.

Results of the nonlinear model in Figure 3(b) show qualitatively similar open-loop strain responses when compared to the linear model in Figure 3(a), and the critical gust length predicted by the nonlinear simulations is also 20m. Oscillations in the nonlinear model appear more highly-damped than in the linear case at this temporal discretization despite both models having the same Newmark damping (0.5%); this is probably due to staggering of aerodynamic and structural solutions in the nonlinear simulation. A final test of the critical gust response at a fine spatial and temporal discretization ($M = 16, N = 40, \Delta t = 8.164 \times 10^{-4}$ s) shows that the nonlinear and linear models are effectively converged (Figure

4).

B. Obtaining Reduced-Order Models

Model-order reduction of the linear system was performed using standard balanced realization and truncation as described in Sec. II.D above. The flap deflection, β, was chosen as the sole control input to the system, and the root bending and torsional strains were chosen as the outputs. The quality of reduced models of various model orders was assessed by comparing their relative time- and frequency-domain forced responses. Time-domain wing responses to flap oscillations at 15 and 30 rad·s^{-1} are shown in Figure 5. Here the nonlinear and full-order linear response is very similar in both the 15 rad·s^{-1}, Figure 5(a), and 30 rad·s^{-1}, Figure 5(b), cases. The reduced-order model with 10 states is shown to approximate the forced response of the system well in both cases too, however when the model order is reduced to 8 states discrepancies are observed in the magnitude and phase of the predicted oscillations, as shown in Figures 5(a) and 5(b).

To further investigate the characteristics of the reduced models they were subjected to frequency-domain forced response analysis. Bode plots of the response of a range of reduced models are shown in Figure. 6 with the model order varied from 8 to 100 states. The reduced frequency shown on the horizontal axes is defined as $k = \omega_\beta c/2U_\infty$, where ω_β is the flap angular velocity and U_∞ is the free-stream flow velocity. For reduced systems of size 10 to 100 the gain and phase plots are very similar up to a reduced frequency of approximately 1.5. The 8 state model shows departures in gain and phase from the higher-order models even at low reduced frequencies which seems to corroborate the relatively poor time-domain comparison in Figure 5. Despite these discrepancies, the 8 state model is still suitable for control synthesis, as the results of the following section demonstrate.

C. Closed-Loop Response

In this section predictive and LQR control schemes formulated with an 8 state reduced model, which provides a compromise between fidelity and performance, are applied to the nonlinear plant simulation. Unless otherwise stated the closed-loop response of the plant under MPC was obtained using $H = 100$ steps in the prediction horizon. The reference conditions on both the states and control inputs is the origin, hence the control systems are designed to provide state regulation. In addition input constraints are specified that correspond to maximum flap deflections of ± 10 deg.

The first control schemes applied here are based on unit weighting of the plant states and inputs, i.e the matrices P, Q and R in Eqs. (16) and (21) are identity matrices. The open- and closed-loop responses, using both MPC and LQR, to the critical gust are shown in

Figure 7. Regulating the model states serves to reduce peak torsional strain with either MPC or LQR by approximately 25% with a corresponding increase in maximum bending strain of approximately 13%. The control action required to produce these results is shown in Figure 8. While the LQR controller is forced into saturation for two periods at the start of the gust response, the MPC controller achieves comparable performance without reaching the input constraints. This is possible because the MPC controller can anticipate future constraint violations and provide an optimal control response that acknowledges the presence of these constraints. In offline design of linear controllers tuning is typically used to ensure bounds on states and inputs for some worst case scenario, however in MPC they are included in the online optimization of Eqs. (16) - (20), thus providing superior closed-loop performance.

The second and third control schemes demonstrated in this work are MPC schemes based on unit weighting of the system outputs, i.e bending and torsional strains, and unit weighting of bending strain alone. In both cases the control inputs are also given unit weighting. The results of Figure 9 demonstrate that the closed-loop performance of system can be effectively tuned using this output weighting. If both outputs are weighted then a 2% reduction in peak bending strain was observed alongside 8% reduction in peak torsional strain. If reduction of peak bending is prioritized then a 10% reduction is realized using unit weighting on bending strain alone, however there is a relatively large corresponding increase in torsional strain.

Finally the timing characteristics of the aforementioned MPC schemes are explored. Since the optimization of Eqs. (16) - (20) must be solved online, it should be guaranteed to have a time-to-solve that is less than the sample time of the system. Figure 10 shows the minimum, maximum and mean times taken to solve the MPC control problem using muAO-MPC[28] generated, single-thread C-code accessed through a Python interface on a 2.93GHz Intel© Core™ i7 desktop CPU. A range of prediction horizons were investigated resulting in varying closed-loop performance and an increase in time-to-solve as the prediction horizon is increased. Using a horizon of 60 steps gives acceptable closed-loop performance with a mean time-to-solve of 1.31 ms, although there were occasional maxima reaching up to 2.9 ms. These results are very much hardware dependent and superior performance would likely be achieved using hardware designed specifically for the task. It is also worth noting that the system used to compute the control response was running an operating system and the nonlinear plant simulation at the same time, which probably contributed to some of the maxima observed in controller time-to-solve. While the Goland wing is relatively stiff it can be expected that the structural response of very flexible aircraft will be an order of magnitude lower in frequency, which is advantageous for control system design and operation. However, this comes at the cost of increased geometric nonlinearity in the plant due to larger dynamic deformations. An extension of this work will aim to address such problems.

V. Conclusions

Nonlinear, linearized, and reduced-order linear models obtained through balanced realization and truncation have been generated to describe the dynamics of a flexible cantilever wing. The forced response of nonlinear, linear and reduced-order models to excitations of a trailing-edge flap was found to be in good agreement, with the only deviations in predicted dynamics occurring when the size of the coupled aeroelastic model was reduced as low as 8 states. Despite these deviations the 8 state reduced model was successfully used to generate effective linear quadratic regulators and predictive controllers which were subsequently applied to nonlinear simulations of the plant dynamics, thus providing a compromise between fidelity and performance. Model predictive control (MPC) was found to give superior closed-loop response in the presence of input constraints compared to an equivalent linear quadratic regulator implemented with input saturation. Timing characteristics of the MPC scheme were investigated and it was found that good closed-loop performance was possible with a corresponding time-to-solve of $\mathcal{O}(1)$ ms using desktop-based hardware and software. Although the mean time-to-solve, 1.31 ms, was less than the system sample time of the relatively stiff test case, 1.633 ms, there is almost certainly too small a margin left to accommodate state-estimation and implementation latency in a real implementation, mostly because of the relatively high frequency dynamics of the wing studied. However, since the dynamics of flexible aircraft are typically an order of magnitude lower in frequency than this example is expected that similarly effective control schemes will be practicable in such cases.

References

[1]van Schoor, M. C. and von Flotow, A. H., "Aeroelastic Characteristics of a Highly Flexible Aircraft," *Journal of Aircraft*, Vol. 27, No. 10, 1990, pp. 901 – 908.

[2]D.H., B., Chen, P., and Panza, J., "Unified Aeroelastic and Flight Dynamic Formulation via Rational Function Approximations," *Journal of Aircraft*, Vol. 43, No. 3, May-June 2006, pp. 763–772.

[3]Su, W. and Cesnik, C. E. S., "Dynamic Response of Highly Flexible Flying Wings," *AIAA Journal*, Vol. 49, No. 2, 2011, pp. 324 – 339.

[4]Karpel, M., "Procedures and models for aeroservoelastic analysis and design," *Zeitschrift fur Angewandte Mathematik und Mechanik*, Vol. 81, No. 9, 2001, pp. 579 – 592.

[5]Noll, T. E., Brown, J. M., Perez-Davis, M. E., Ishmael, S. D., Tiffany, G. C., and Gaier, M., "Investigation of the Helios Prototype Aircraft Mishap," Mishap Report: Volume 1, NASA, Jan. 2004.

[6]Rawlings, J. B. and Mayne, D. Q., *Model Predicitive Control: Theory and Design*, Nob Hill Publishing, 1st ed., 2009.

[7]Maciejowski, J. M., *Predicitive Control with Constraints*, Pearson Education, 1st ed., 2001.

[8]Giesseler, H.-G., Kopf, M., Varutti, P., Faulwasser, T., and Findeisen, R., "Model Predictive Control for Gust Load Alleviation," *4th IFAC Nonlinear Model Predicitive Control Conference*, International Federation of Automatic Control, Noordwijkerhout, NL, Aug. 2012.

[9]Haghighat, S., Liu, H. H. T., and Martins, J. R. R. A., "Model-Predictive Gust Load Alleviation

Controller for a Highly Flexible Aircraft," *Journal of Guidance, Control, and Dynamics*, Vol. 35, No. 6, 2012, pp. 1751 – 1766.

[10]Cook, R., Palacios, R., and Goulart, P., "Robust Gust Alleviation and Stabilization of Very Flexible Aircraft," *AIAA Journal*, Vol. 51, No. 2, February 2013, pp. 330–340.

[11]Dillsaver, M., Cesnik, C., and Kolmanovsky, I., "Gust Load Alleviation Control for Very Flexible Aircraft," *AIAA Atmospheric Flight Mechanics Conference*, Minneapolis, Minnesota, August 2011.

[12]Hodges, D. H., "A mixed variational formulation based on exact intrinsic equations for dynamics of moving beams," *International Journal of Solids and Structures*, Vol. 26, No. 11, 1990, pp. 1253 – 1273.

[13]Géradin, M. and Cardona, A., *Flexible Multibody Dynamics: A Finite Element Approach*, John Wiley & Sons Ltd, Chichester, UK, 2001.

[14]Hesse, H. and Palacios, R., "Consistent structural linearisation in flexible-body dynamics with large rigid-body motion," *Computers & Structures*, Vol. 110 - 111, 2012, pp. 1–14.

[15]Stevens, B. L. and Lewis, F. L., *Aircraft Control and Simulation*, John Wiley & Sons, Inc., New York, NY, USA, 1992.

[16]Murua, J., Hesse, H., Palacios, R., and Graham, J. M. R., "Stability and Open-Loop Dynamics of Very Flexible Aircraft Including Free-Wake Effects," *52nd AIAA/ASME/ASCE/AHS/ASC Structures, Structural Dynamics and Materials Conference*, Denver, Colorado, April 2011.

[17]Morino, L. and Bernardini, G., "Singularities in BIEs for the Laplace equation; Joukowski trailing-edge conjecture revisited," *Engineering Analysis with Boundary Elements*, Vol. 25, No. 9, Oct. 2001, pp. 805 – 818.

[18]Katz, J. and Plotkin, A., *Low-Speed Aerodynamics*, Cambridge University Press, 2001.

[19]Wang, Z., Chen, P. C., Liu, D. D., and Mook, D. T., "Nonlinear-Aerodynamics/Nonlinear-Structure Interaction Methodology for a High-Altitude Long-Endurance Wing," *Journal of aircraft*, Vol. 47, No. 2, 2010, pp. 556 – 566.

[20]Murua, J., *Flexible Aircraft Dynamics with a Geometrically-Nonlinear Description of the Unsteady Aerodynamics*, Ph.D. thesis, Imperial College London, Department of Aeronautics, May 2012.

[21]Simpson, R. J. S. and Palacios, R., "Numerical aspects of nonlinear flexible aircraft flight dynamics modeling," *54th AIAA/ASME/ASCE/AHS/ASC Structures, Structural Dynamics, and Materials Conference*, AIAA, Boston, MA, April 2013.

[22]Simpson, R. J. S., Palacios, R., and Murua, J., "Induced Drag Calculations in the Unsteady Vortex-Lattice Method," *AIAA Journal*, 2013, Accepted for publication.

[23]Géradin, M. and Rixen, D., *Mechanical vibrations: theory and application to structural dynamics*, John Wiley, Chichester, UK, 2nd ed., 1997.

[24]Murua, J., Palacios, R., and Graham, J. M. R., "Applications of the unsteady vortex-lattice method in aircraft aeroelasticity and flight dynamics," *Progress in Aerospace Sciences*, Vol. 55, Nov. 2012, pp. 46 – 72.

[25]Hall, K. C., "Eigenanalysis of unsteady flows about airfoils, cascades, and wings," *AIAA journal*, Vol. 32, 1994, pp. 2426 – 2432.

[26]Moore, B., "Principal component analysis in linear systems: Controllability, observability, and model reduction," *IEEE Transactions on Automatic Control*, Vol. 26, No. 1, 1981, pp. 17–32.

[27]Glover, K., "All optimal Hankel-norm approximations of linear multivariable systems and their L^∞-error bounds," *International Journal of Control*, Vol. 39, No. 6, 1984, pp. 1115 – 1193.

[28]Zometa, P., Kögel, M., and Findeisen, R., "muAO-MPC: A Free Code Generation Tool for Embedded Real-Time Linear Model Predictive Control," *Proc. American Control Conference (ACC), 2013*, Washington D.C., USA, 2013, pp. 5340–5345.

[29]Goland, M., "The Flutter of a Uniform Cantilever Wing," *Journal of Applied Mechanics*, Vol. 12, No. 4, Dec. 1945, pp. A197 – A208.

[30]Goland, M. and Luke, Y. L., "The flutter of a uniform wing with tip weights," *Journal of Applied Mechanics*, Vol. 15, No. 1, March 1948, pp. 13 – 20.

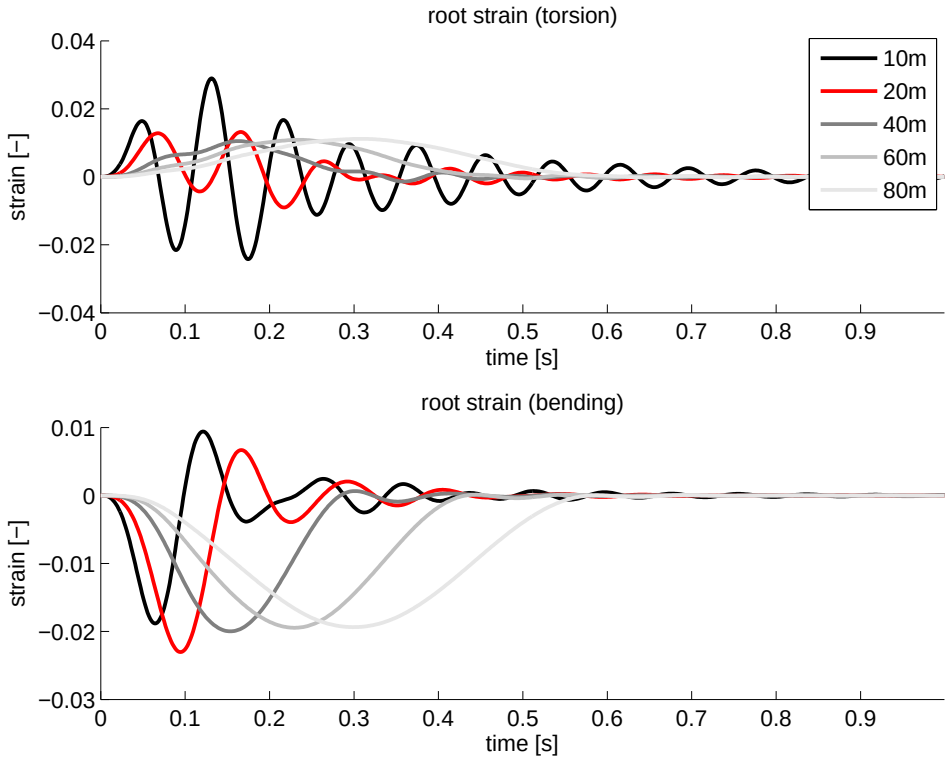

(a) full-order linear model

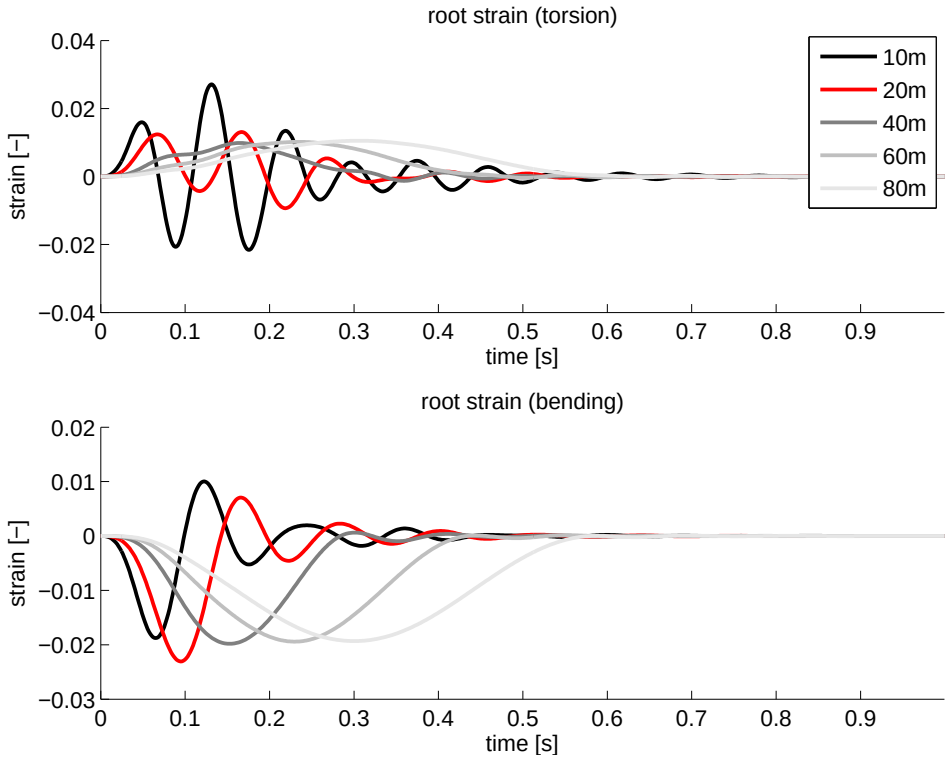

(b) nonlinear model

Figure 3. Open-loop gust response at a range of gust lengths.

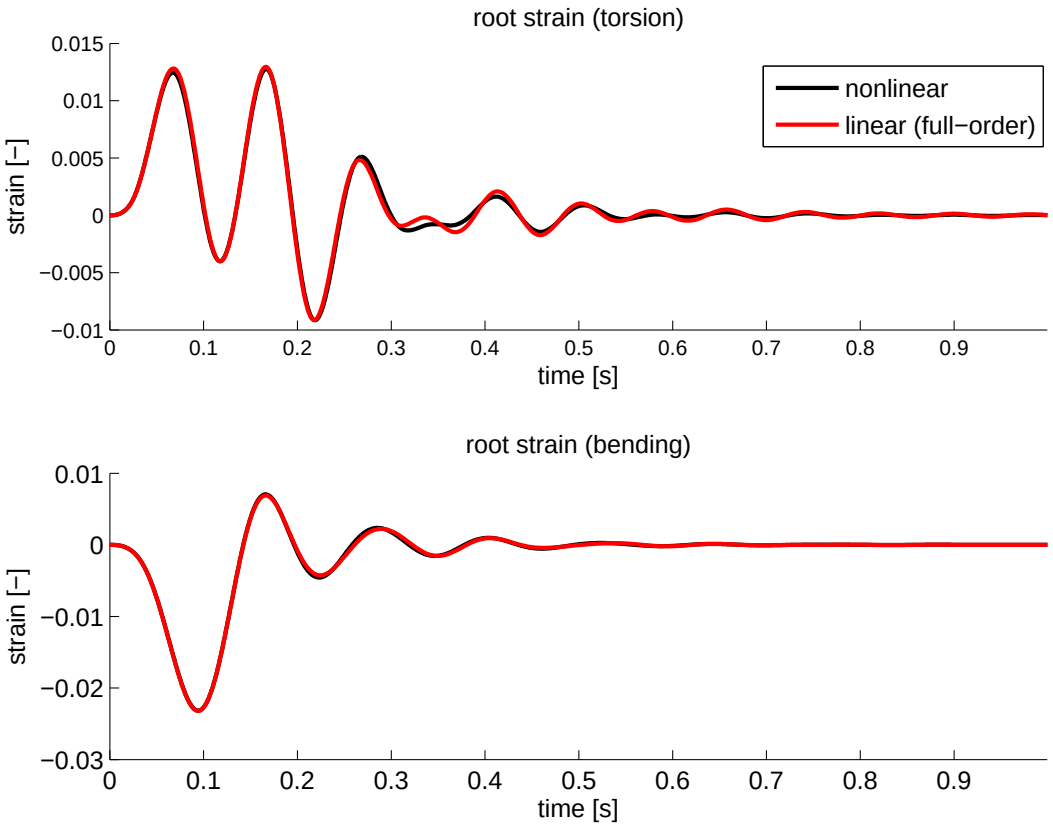

Figure 4. Comparison of linear and nonlinear models for the critical gust length, $L = 20\text{m}$.

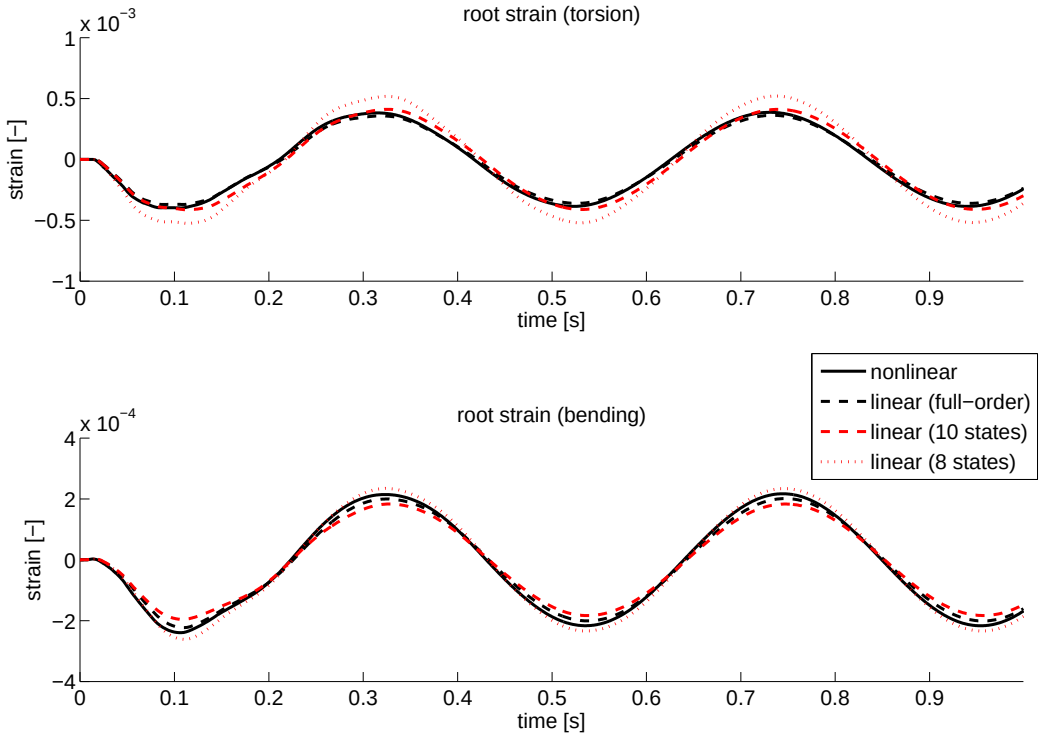

(a) $\omega_\beta = 15$ rad·s^{-1}

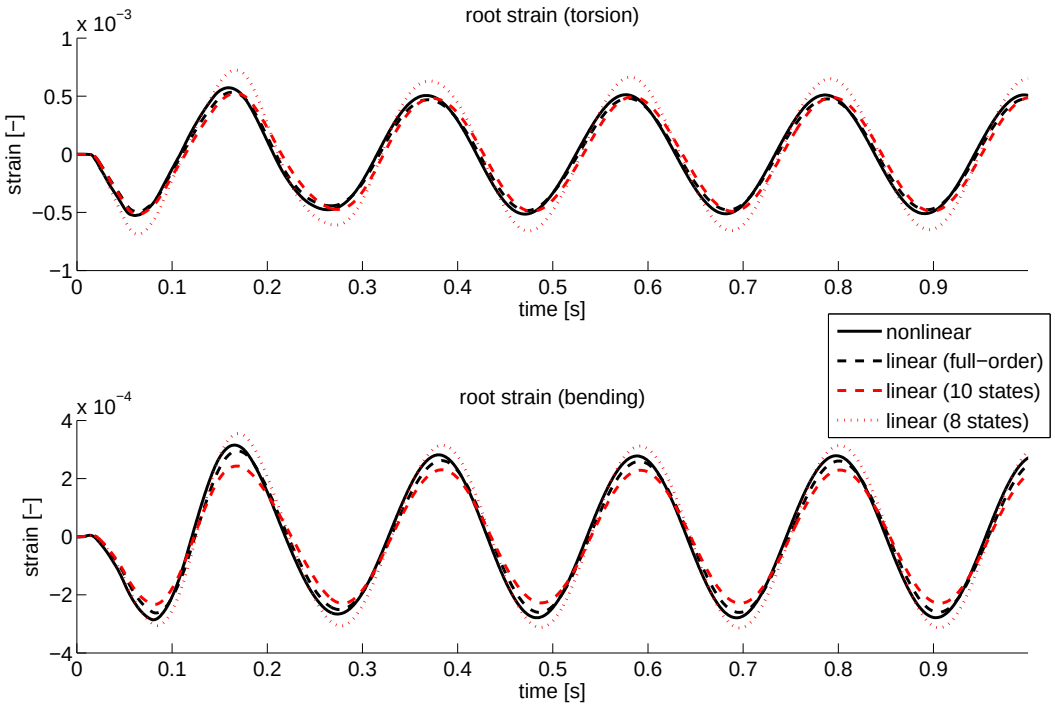

(b) $\omega_\beta = 30$ rad·s^{-1}

Figure 5. Time-domain forced response of nonlinear, full-order linear and reduced-order linear models.

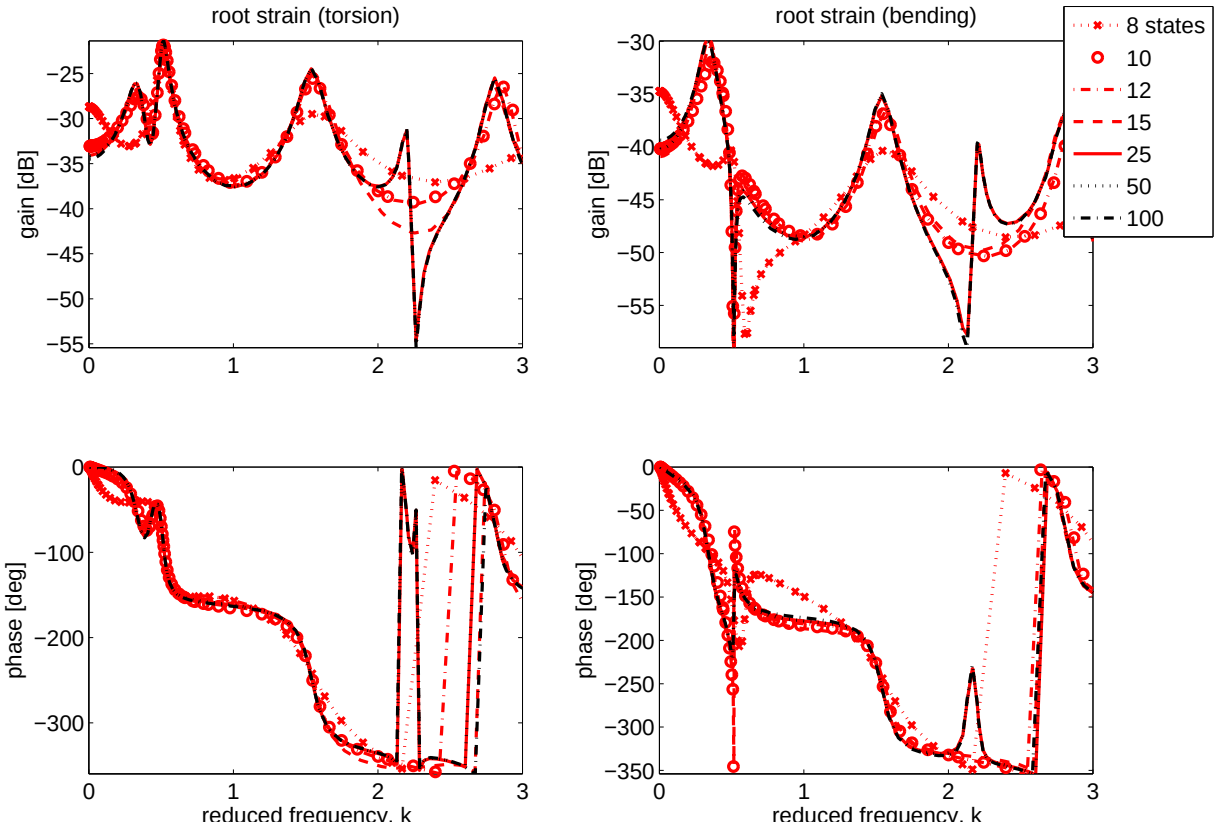

Figure 6. Frequency response of a range of reduced-order linear models with varying number of states.

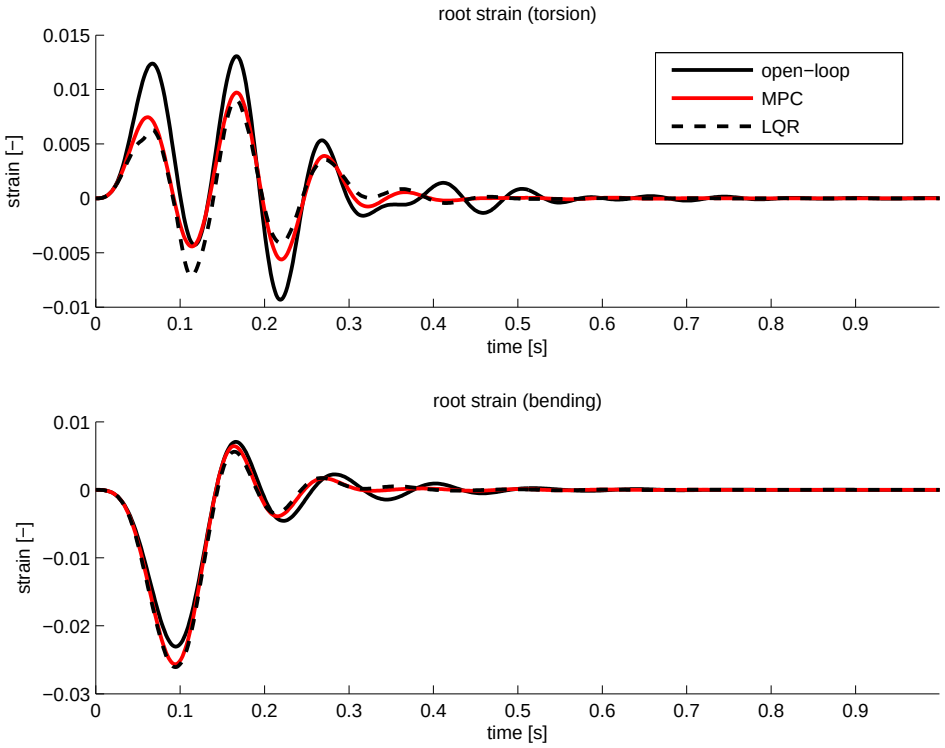

Figure 7. Gust load alleviation using MPC and LQR with unit weighting on the reduced states and inputs. Regulating the model states serves to reduce peak torsional strain with a corresponding increase in bending.

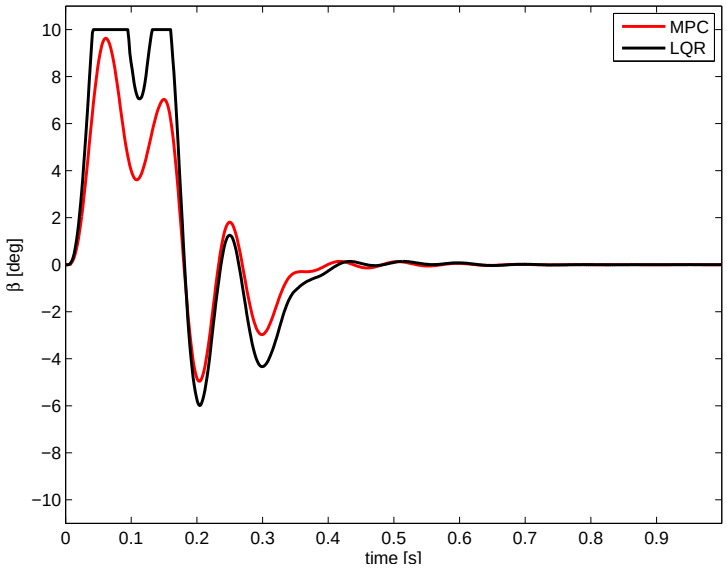

Figure 8. Control response commanded in response to critical gust with unit weighting on the reduced states and inputs.

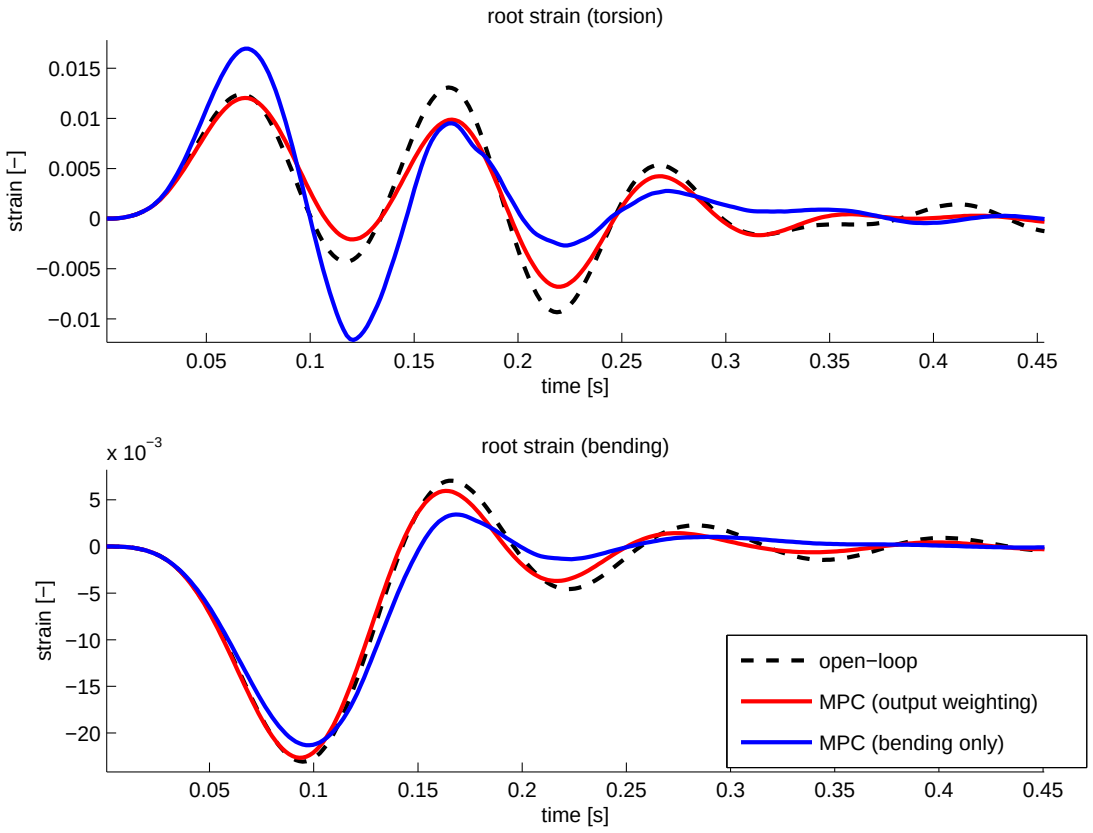

Figure 9. Closed-loop performance for critical gust when unit weighting on the reduced system outputs is used (red line), and when only the bending strain is prescribed unit weighting (blue line).

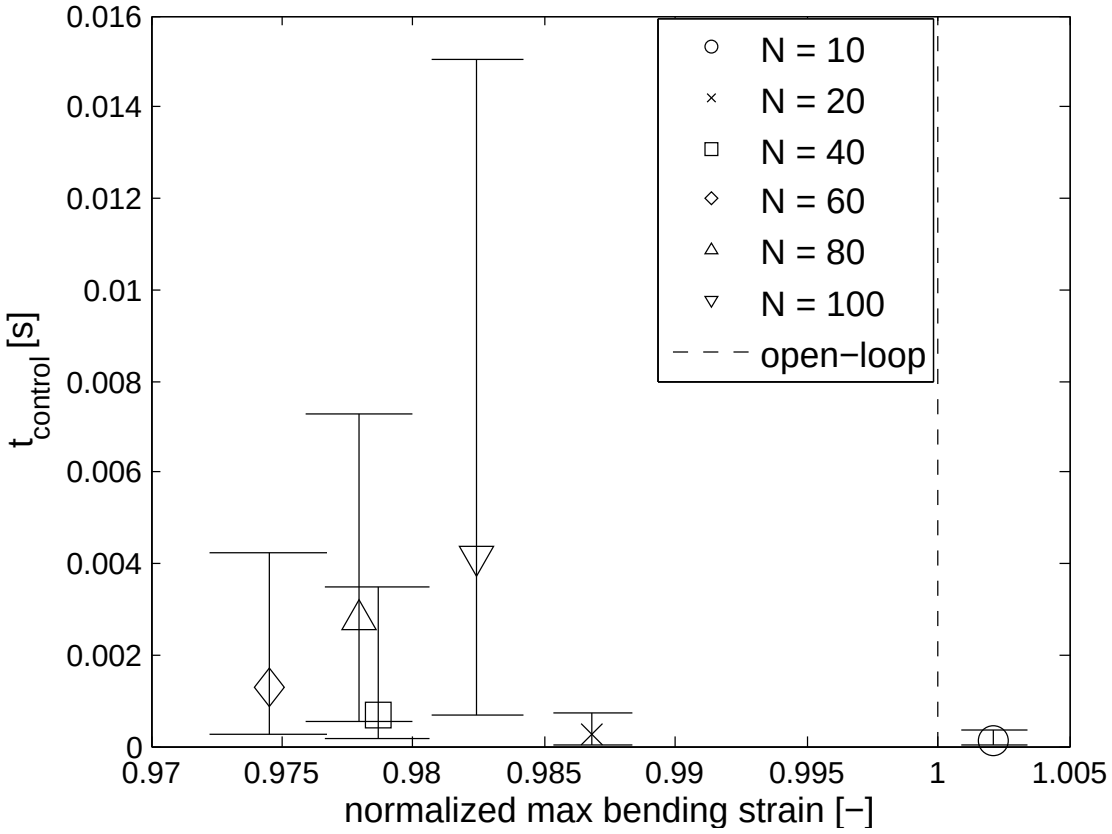

Figure 10. Minimum, maximum and mean time taken to solve the online MPC problem for a range of horizon lengths, plotted against closed-loop performance. In this case unit weighting was prescribed to the system outputs and input.